Journal of
Materials Chemistry C

ROYAL SOCIETY
OF CHEMISTRY

PAPER

View Article Online
View Journal | View Issue

Check for updates

Cite this: *J. Mater. Chem. C*, 2020, **8**, 11525

A highly sensitive piezoresistive sensor with interlocked graphene microarrays for meticulous monitoring of human motions†

Lin Cheng,‡[a] Wei Qian,‡[a] Lei Wei,[a] Hengjie Zhang,[b] Tingyu Zhao,[a] Ming Li,[c] Aiping Liu *[ade] and Huaping Wu *[b]

Received 28th May 2020,
Accepted 4th July 2020

DOI: 10.1039/d0tc02539a

rsc.li/materials-c

The development of flexible sensors with high sensitivity and a short response time has received great attention due to their potential applications in medical diagnosis and health monitoring. Herein, we demonstrate the design of a flexible piezoresistive sensor based on interlocked graphene microarrays on a flexible substrate. This sensor displays adjustable piezoresistance by changing the contact way of the graphene microarrays *via* micromanipulation, which endows the sensor with desirable compression sensitivity (10.41 kPa^{-1}, <2.5 kPa), a fast response time (<19 ms), a broad measurement range (1.0 Pa–32 kPa) and excellent durability ($>10\,000$ loading–unloading cycles). In particular, the fast-response characteristic of this sensor allows meticulous detection of complicated stimuli from various human motions by obviously changing the contact areas between the interlocked graphene microarrays when compared with a planar sensor with double-layered graphene films and a single microarray sensor, highlighting its potential application in wearable healthcare systems for more comprehensive and accurate analysis.

1. Introduction

Skin-like strain sensors with excellent stretchability, flexibility and sensitivity have received great attention because of their promising applications in wearable healthcare systems,[1,2] human–machine interfaces,[3,4] robotics,[5–7] prosthetic devices[8] and intelligent medical diagnosis.[9,10] These strain sensors can convert mechanical deformations into detectable electronic signals according to different sensing mechanisms (including capacitive, piezoelectric, triboelectric, and resistive sensing) at various states of stretching, compression, shear or bending.[11,12] Among them, the piezoresistive sensor, which converts applied pressure and strain into electrical resistance variation, has been widely investigated because of its advantages of a simple structure, simple system for signal readout, and low-cost device fabrication. Flexible piezoresistive sensors composed of electrically conductive sensing elements (such as metals and carbon materials) and dielectric elastomers (such as polydimethylsiloxane (PDMS) and Ecoflex) can realize the detection of strain/pressure stimuli by the change of contact resistance between the conductive elements.[13,14] Among carbon materials, graphene possesses unique superiorities such as good electrical conductivity, intrinsic and structural flexibility, high chemical and thermal stability, low toxicity, easy chemical functionalization, and potential mass production, making it a promising candidate material for wearable strain/pressure sensors.[15–17]

Additionally, recent progress on the controlled geometrical design of flexible sensors by introducing bioinspired micro/nanostructures and 2D/3D structures is more encouraging for the effective transduction of external stress into electrical signals.[18] Many studies have been conducted to improve the multifunctional sensing properties of flexible electronic skin, such as sensitivity, selectivity, response time and mechanical compliance.[19,20] For example, bio-inspired micro/nanostructures including interlocking,[21,22] hierarchical,[23,24] crack,[25] whisker[26] and fingerprint structures[27] and 2D/3D structures such as wrinkle,[28,29] serpentine,[30] pyramid,[31] dome[32] and porous structures[33] have been designed for the improvement of sensor performance due to the large variation of the contact area or the effective stress concentration at the contact points of the adjacent interlayers, resulting in

---

[a] *Center for Optoelectronics Materials and Devices, Key Laboratory of Optical Field Manipulation of Zhejiang Province, Zhejiang Sci-Tech University, Hangzhou 310018, P. R. China. E-mail: liuaiping1979@gmail.com*

[b] *Key Laboratory of Special Purpose Equipment and Advanced Processing Technology, Ministry of Education and Zhejiang Province, College of Mechanical Engineering, Zhejiang University of Technology, Hangzhou 310023, P. R. China. E-mail: wuhuaping@gmail.com*

[c] *State Key Laboratory of Structural Analysis for Industrial Equipment, Dalian University of Technology, Dalian 116024, China*

[d] *State Key Laboratory for Strength and Vibration of Mechanical Structures, School of Aerospace Engineering, Xi'an Jiaotong University, Xi'an 710049, P. R. China*

[e] *State Key Laboratory of Digital Manufacturing Equipment and Technology, Huazhong University of Science and Technology, Wuhan 430074, P. R. China*

† Electronic supplementary information (ESI) available. See DOI: 10.1039/d0tc02539a

‡ L. Cheng and W. Qian contributed equally to this work.

enhanced sensitivity to multidirectional stress and static/dynamic mechanical stimuli.

Here, we demonstrate a flexible piezoresistive pressure sensor with adjustable interlocked graphene micropillars wrapped on elastomeric PDMS arrays obtained using microfabrication and micromanipulation technologies. Furthermore, the structural design of the sensor with an optimized interlocked manner offers the advantages of a broad pressure detection range and satisfactory sensitivity (1.0 Pa–32 kPa with a sensitivity of 10.41 kPa^{-1} below 2.5 kPa), excellent durability (more than 10 000 cycles), a rapid response (<19 ms) and a short relaxation time (<10 ms) as compared with planar sensors with double-layered graphene films and single microarray sensors due to the immediate pressure-induced variation of the contact area between interlocked graphene micropillars under different static loadings. In particular, we demonstrate that our sensor can be utilized to detect both static and dynamic mechanical stimuli due to the piezoresistive properties of graphene. The rapid response also enables the interlocked pressure sensor to elaborately monitor various human motions, suggesting its potential in wearable healthcare systems for more comprehensive and accurate analysis.

2. Materials and methods

2.1 Fabrication of the interlocked piezoresistive sensor

The silicon mold with micropillar arrays prepared using microfabrication technology was first treated with a H_2SO_4 and H_2O_2 mixed solution (volume ratio of 3 : 1) at 90 °C in a water bath, washed with deionized water and hydrophobically treated with a mixture of *n*-heptane (93 wt%), eighteen-alkyl-alkoxy silane (2 wt%) and ethyl acetate (5 wt%). Then, a mixture of the PDMS precursor and the curing agent (weight ratio of 10 : 1, Sylgard 184, Dow Corning) after removing air bubbles was poured onto the microstructured silicon molds and cured at 80 °C for 90 min, obtaining the PDMS mold with a microstructure after peeling it off from the silicon mold. The as-prepared PDMS mold was further hydrophilized by a treatment of oxygen plasma spurting and poly(diallyldimethylammonium chloride) (PDDA, 5 wt%) modification. After that, a graphene solution (Nanjing Xianfeng Ltd, 0.3 mg mL^{-1}) was drop coated onto the microstructured PDMS surface and desiccated at 40 °C for 5 hours. In order to construct the interlocked structure of the flexible pressure sensor, two PDMS films with graphene micropillars (copper wires extracted on each side of graphene) were bonded face-to-face using micromanipulation technology. Two kinds of contact forms were designed, the non-interlocked interposition and the side-contact interlock. In order to better understand the working mechanism of the interlocked pressure sensors, a planar sensor with double-layered graphene films and a single microarray sensor were also fabricated by controlling the same drop-coating amount of graphene solution.

2.2 Characterization

The morphology and microstructure of the piezoresistive sensor were investigated by using field emission scanning electron microscopy (FE-SEM, Hitachi S4800) and a Raman spectrometer (Thermo Fisher DXR) equipped with an objective (50×) using a He–Ne laser (λ = 632.8 nm). The crystalline structure of graphene was characterized using X-ray diffraction (XRD, Bruker AXS D8) using Cu Kα radiation (λ = 0.154 18 nm) with the 2θ scan from 10° to 80° at a step of 0.2°. The sheet resistance of the graphene layers on the PDMS matrix was measured using a four-point-probe method using a Keithley 4200 sourcemeter. The real-time tests of the electromechanical properties of the piezoresistive sensors were carried out by using a Keithley 4200 sourcemeter with a two-probe measurement system. The surfaces of the graphene layers were coated with silver paste and connecting copper wires were used.

2.3 Simulation

In order to explore the sensing mechanism, finite element statics analysis was performed with the commercial package ABAQUS when the interlocking of graphene micropillars happened under an external force. For the micro-column covered with graphene (a diameter of 16 μm, a height of 20 μm and a spacing of 30 μm in the unit cell with a size of 1 cm × 1.5 cm), stress ranging from 0 to 30 kPa was applied in the normal direction of the unit cell. The micro-column produced elastic strain and thus the relationship between the contact area and external stress was obtained. The material parameters used in the simulation were taken from ref. 34.

3. Results and discussion

3.1 Microstructure of the interlocked piezoresistive sensor

A schematic of the fabrication process of the interlocked pressure sensor is demonstrated in Fig. 1(a). The PDMS elastomer with micropillar arrays was obtained by micromolding a liquid mixture of PDMS and a curing agent into a silicon mold and subsequently peeling off after solidification. The micromolding process produces a flexible smooth PDMS film with regular micropillar arrays, typically characterized by a height of 20 μm, a diameter of 16 μm, and a pitch of 30 μm (Fig. 1c). Hydrophilic treatment of the PDMS film enables graphene to easily spread across the PDMS surface to form a uniformly wrinkled film (Fig. 1d, the wrinkles of the graphene film can be clearly noticed from the high magnification image in Fig. 1e) by virtue of the increased number of carboxyl groups formed after plasma oxygen etching[35] and positive charges created after PDDA modification, which promotes the adsorption of graphene with negative charges.[36] For the fabrication of the

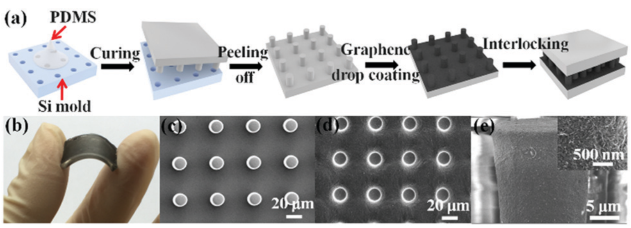

Fig. 1 (a) Diagram showing the fabrication of the piezoresistive sensor with interlocked graphene microarrays. (b) A photo of the flexible piezoresistive sensor with interlocked graphene microarrays. (c) SEM image of the PDMS elastomer with micropillar arrays. (d) SEM image of the PDMS elastomer with graphene drop-coated on it. (e) SEM image of a single graphene micropillar. The inset clearly shows the wrinkles of the graphene films.

highly flexible piezoresistive sensor (Fig. 1b), two PDMS elastomers with graphene micropillar arrays were combined with the patterned sides facing each other (Fig. 1a) using micromanipulation technology, producing an interlocked geometry of micropillar arrays. To characterize the absorption of graphene on the PDMS film, XRD and Raman measurements were carried out before and after graphene film formation. The apparent peak at 23.5° in the XRD pattern of the graphene film is related to the (002) diffraction peak of graphene (Fig. S1a, ESI†).[37] The Raman characteristic peaks of PDMS at 1260 cm^{-1} and 1411 cm^{-1} move to 1344 cm^{-1} and 1580 cm^{-1},[38] indicating the successful attachment of graphene on the PDMS surface (Fig. S1b, ESI†).

3.2 Piezoresistive performance of the interlocked pressure sensor

Flexible piezoresistive sensors can distinguish various directional stimuli, for instance, normal, stretching, shear and bending forces. When an external force (normal, shear and bending) is applied to the sensor with the side-contact interlock, deformation of the pillar structures will be induced due to their side slipping and extrusion (Fig. 2a), resulting in an increase of the contact area between the micropillar arrays. This would cause the device to experience a decrease in resistance, leading to an increased current (Fig. 2b). When the external force is released, the micropillar structures would recover to their initial status due to the elastic properties of PDMS, resulting in a decreased current. For the case of the stretching stimulus, the maximum principal strain will increase with the tensile force (Fig. S2a, ESI†), and some microcracks might form on the upper and lower graphene layers, which could result in an increased resistance and a reduced current (Fig. 2b). Under a shear force, there is a significant Mises stress only at the base of the micropillars (Fig. S2b, ESI†). Though the bending force might cause microcracks on the upper graphene layer to form, the maximum principal strain is relatively smaller when compared to that of the stretching stimulus (Fig. S2c, ESI†), and the effect of lateral slip and extrusion between pillars is predominant. The two kinds of contact forms, namely side-contact interlock and non-interlock interposition, are shown in Fig. 2d. The signals obtained from the former (Fig. 2b) are larger than those obtained from the latter (Fig. 2c). This could be attributed to the more complicated side contact and the larger increment of contact area for the side-contact interlocked sensor. For example, there could be lateral slip, extrusion and even separation between micropillars for the side-contact interlocked sensor under the bending force (Fig. S3a, ESI†), and the increment of contact area is really quite obvious (Fig. S3b, ESI†). When a bending force is applied to the sensor with the non-interlock interposition, this state is more akin to that of the stretching one due to the lack of lateral friction and extrusion, presenting a small maximum principal strain, negligible area changes and a decreased current (Fig. S2d and Fig. S3b (ESI†) and Fig. 2c).

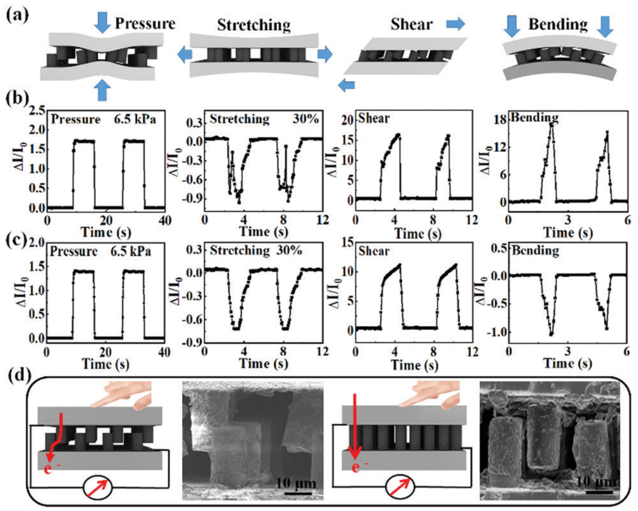

Fig. 2 (a) Schematic of the stress-detection-sensitive pressure sensor for various mechanical stimuli such as pressure, stretching, shear and bending. (b and c) Relative current changes of the pressure sensor under different mechanical stimuli: (b) the side-contact interlock way and (c) the non-interlock interposition way. (d) Schematic diagram and SEM images of the sensors with side-contact interlock and non-interlock interposition ways.

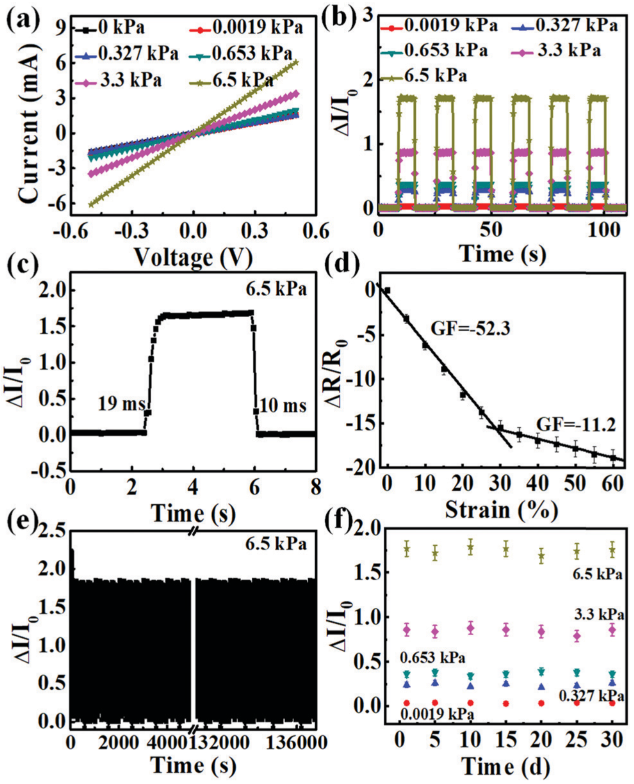

Fig. 3 (a) Current–voltage curves and (b) relative current changes of the interlocked pressure sensor at different pressure loadings. (c) The response time and relaxation time of the interlocked pressure sensor at a loading of 6.5 kPa. (d) The relative change in resistance *versus* compressive strain of the interlocked sensor. The slopes of the plot were the gauge factor (GF). (e) The stability test of the sensor over 10 000 loading–unloading cycles under an applied pressure of 6.5 kPa. (f) The durability test of the sensor at different times under different applied pressures. (The sensor was kept sealed for further use after 1000 cycles at a given pressure and time.) The error bar was the standard deviation.

Fig. 3a displays the noise-free and stable continuous responses of the side-contact interlocked sensor at various pressure loads. The conductivity of the graphene layers on the PDMS matrix is about 3.2×10^{-3} S cm^{-1}. The linear character of the current–voltage curves indicates that the device obeys Ohm's law, and the resistance exhibits an obvious decrease as external pressure increases (Fig. 3b). The pressure sensor exhibits a very rapid response ($<$19 ms) and a short relaxation time ($<$10 ms) (Fig. 3c). This is better than those of previously reported resistive pressure sensors for electronic skin[39–41] (Table S1, ESI†) and human finger perception time (30–50 ms).[24,42] By comparison, the double-layer planar sensors without interlocked structures and the single microarray sensors in our reference experiment presented inferior piezoresistive behaviors with a smaller current change at the same pressure loads (Fig. S4a and b, ESI†) and a slower response time (Fig. S4c and d, ESI†). The gauge factor (GF) defined as the relative change of resistance ($\Delta R/R_0$) to the applied strain (ε) under compressive conditions (GF = $(\Delta R/R_0)/\varepsilon$) was also obtained from the slope of the plot shown in Fig. 3d. Here, R_0 was the resistance under zero strain. By linear fitting, the GF value was calculated to be −52.3 and −11.2 in the 0–30% and 30–60% strain ranges, respectively. We ascribe the two linear regions to the contact-resistance effect. In the first strain range, the graphene pillars undergo lateral slip and extrusion upon pressure, increasing the contact area and decreasing the contact resistance. However, in the second strain range, a stable lateral contact would form, which leads to a dramatic decrease in the GF. The durability and stability of the piezoresistive pressure sensor were investigated through repeated loading–unloading cycling tests. As shown in Fig. 3e, the output signals of the pressure sensor are stably maintained without any remarkable degradation after repeating the process 10 000 times at 6.5 kPa loading. The piezoresistive characteristics were satisfactory during one-month of repeated testing under different pressures (Fig. 3f). The wrinkled nanostructures of the graphene pillars might be of importance in maintaining the stability and integrity of the flexible piezoresistive sensor, proving it to be highly reproducible and repeatable upon repeated mechanical loading. Additionally, it has been reported that protruding microstructures such as micropillar arrays could be helpful in decreasing crack formation and propagation.[22]

The preponderance of the side-contact interlocked pressure sensor under various stimuli is also demonstrated in its sensitivity, which can be obtained from the slope of the relative current change as a function of the applied pressure (Fig. 4a). A high sensitivity of 10.41 kPa^{-1} is obtained in the low pressure range under 2.5 kPa, which decreases to 1.80 kPa^{-1} in the pressure region of 2.5–32 kPa. This difference of sensitivity in the two consecutive pressure regions could be attributed to the contact area change between the interlocked micropillar arrays. We simulated the process of two pillars contacting by using finite element statics analysis. When an external pressure ($<$2.5 kPa) is imposed on the upper surface of the sensor, a frictional force would be produced at the interface of the side-contact graphene pillars with wrinkles, resulting in a rapid increase in the contact area and an obvious current increase (Fig. 4b). When the pillar tops contact the surface of the graphene film, the frictional force disappears, which drastically reduces the increase rate of the contact area due to the deformation saturation of contacting protuberances of the graphene wrinkles and this generates a gently increased current when the external pressure $>$2.5 kPa. Notice that according to Kim's report, the friction coefficient for the graphene film was about 0.12–0.22.[43] Therefore, we also inspected the effect of the friction coefficient on the incremental area. Our calculated results further confirm the changing trend of area increment in the two consecutive pressure regions (Fig. 4b). Based on the excellent sensitivity, the pressure sensor could reliably detect loads of about 1.0 Pa (considering a water droplet with a weight of ∼15 mg dripped onto the PDMS surface), as shown in Fig. S5 (ESI†), indicating the ultralow detection limit compared with previous pressure sensors.[44,45] By contrast, the piezoresistive performances of the single microarray sensor and the planar sensor without microstructures are inferior with a sensitivity of 1.85 kPa^{-1} ($<$2.5 kPa) and 0.18 kPa^{-1} ($>$2.5 kPa) for the single microarray sensor and 0.83 kPa^{-1} ($<$2.5 kPa) and 0.081 kP^{-1} ($>$2.5 kPa) for the planar sensor, respectively (Fig. 4a). This could be attributed to the weaker pressure-induced surface deformation of the micropillars or the graphene surface, resulting in a tiny variation of the contact area, as shown in the simulation results in Fig. 4c. In addition, the variation of contact area can also be adjusted by changing the interlock way of the sensor (Fig. S6, ESI†). Thus, the interlock way determines the area increment and the pressure sensitivity of the sensor. Therefore, the piezoresistive performance is highly adjustable based on the elaborate design of the sensor devices to achieve the desired sensitivity.

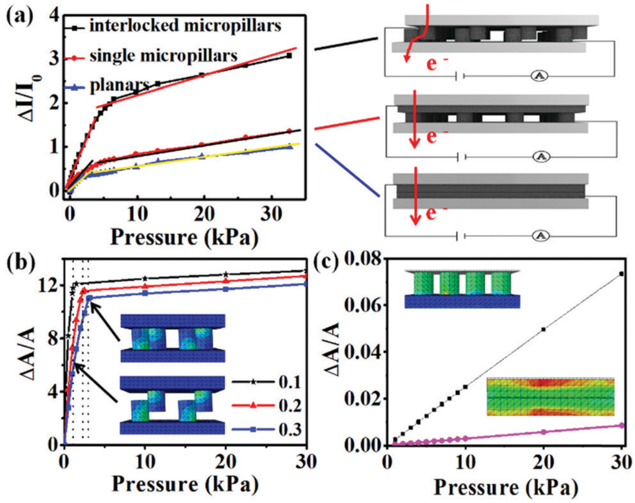

Fig. 4 (a) Pressure sensitivities of different sensors including the interlocked microarray sensor, planar sensor without microstructures and single microarray sensor. (b) The change of area increment with external pressure and stress distribution for the side-contact interlocked sensor. (c) The change of area increment with external pressure and the stress distribution for the planar sensor without microstructures and the single microarray sensor.

3.3 Human motion monitoring by using interlocked pressure sensors

Human motion monitoring was carried out by using the interlocked piezoresistive sensor. When the sensor was tightly attached to the wrist to form a conformal contact, various human hand

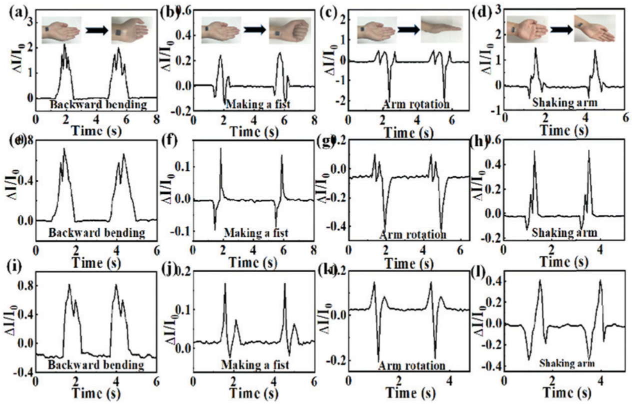

Fig. 5 Stress-direction-sensitive flexible sensors to detect and distinguish various gestures by using the side-contact interlocked sensors: (a) backward bending, (b) making a fist, (c) arm rotation, and (d) shaking the arm. Corresponding hand motions observed using the (e–h) planar sensor with double-layered graphene films and (i–l) the single microarray sensor.

motions such as backward bending, making a fist, arm rotation and shaking the arm could be detected due to the contraction and relaxation of the muscles, as shown in Fig. 5 (also see Movie S1, ESI†). It is surprising that stronger and more elaborate characteristic waveforms related to various wrist motions can be observed by using the interlocked piezoresistive sensor when compared to the planar sensor without microarrays and the single microarray sensor. If we reduce the speed of wrist motion, the characteristic waveforms observed from these three sensors are analogous (Fig. S7, ESI†). This means that the response time of the sensor has an important effect on the real-time detection of quick human motions. The interlocked pressure sensor with a rapid response (<19 ms) and a short relaxation time (<10 ms) (Fig. 3c) is more suitable for wearable healthcare system applications for more comprehensive and accurate analysis.

We further explored the potential of the interlocked pressure sensor for monitoring voice vibrations and pulse signals. When the sensors were attached to the skin of the larynx of three volunteers, they could distinctly discriminate different vibration patterns produced when reading the words "hello", "graphene" and "ZSTU" (the abbreviation for Zhejiang Sci-Tech University). And the more comprehensive vibration curves were also given by the interlocked piezoresistive sensor (Fig. 6). In a similar way, more complete analysis related to cardiorespiratory function is also provided by the interlocked pressure sensor when it is attached to different body parts including arc wrist, carotid artery and the fifth intercostal space (Fig. 7). For wrist pulse, carotid artery and apexcardiogram (ACG), all of them provide the complete information of the systolic and diastolic functions of the heart[46,47] when using the interlocked piezoresistive sensor. Even after strenuous exercise for 5 minutes, the sensor still accurately provides the physiological signals of human heart beating, especially for the ACG technology, which is free from external interference for human heart health monitoring (Fig. S8, ESI†). Therefore, the sensor can be predominantly used in noninvasive and biocompatible wearable voice-monitoring systems and for cardiorespiratory monitoring, medical diagnosis and rehabilitation.

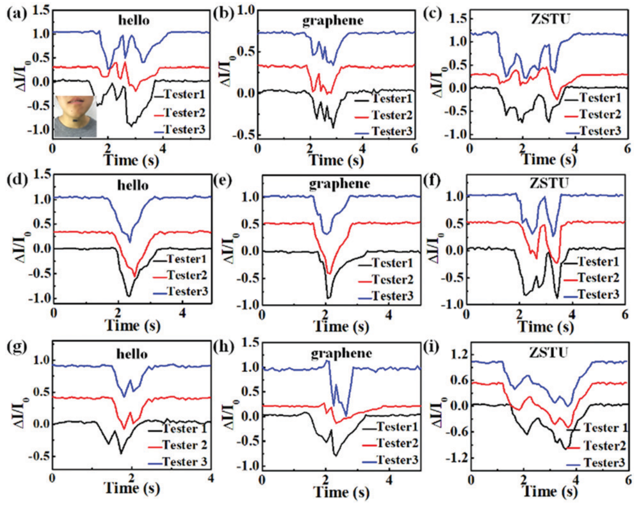

Fig. 6 Real-time monitoring of vocal cord vibrations during speaking. (a–c) The waveforms of "hello", "graphene" and "ZSTU" obtained by using the side-contact interlocked sensor. The inset in (a) is photograph taken during measurement. Corresponding waveforms of vocal cord vibrations obtained by using the planar sensor with double-layered graphene films (d–f) and the single microarray sensor (g–i).

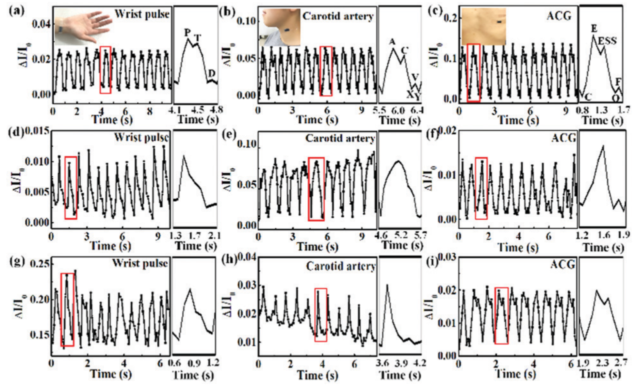

Fig. 7 Real-time monitoring of human basic physiological information. (a–c) Wrist pulse, carotid artery and ACG waves obtained by using the side-contact interlocked sensors. The insets in (a–c) are the photographs taken during measurement with the sensors attached to the (a) wrist, (b) neck and (c) chest. Corresponding physiological information obtained by using the planar sensor with double-layered graphene films (d–f) and the single microarray sensor (g–i).

In addition to detecting static-pressure variations, our sensors were also used to detect dynamic pressure variations. Movie S2 (ESI†) shows the real-time variation in the relative current under a continuous radiofrequency stimulus, which is important for the real-time monitoring of environmental changes.

4. Conclusions

In conclusion, we fabricated highly sensitive and fast-response pressure sensors with interlocked graphene micropillars by using microfabrication and micromanipulation technologies, which led to an adjustable piezoresistance by contact design. The microstructure construction of the flexible piezoresistive pressure sensor provided a sensor with a broad linear response to applied pressure with a fast response time of 19 ms, a low limit of detection of 1 Pa, and a high durability for over 10 000 cycles. The interlocked sensors enabled the sensitive detection of both static and dynamic stimuli through piezoresistive transductions, such as human motions and voice-frequency stimuli. We believe our study will contribute effectually toward the development of advanced pressure sensors that have various applications in multifunctional electronic skin for medical diagnostic tools and wearable human-health monitoring systems.

Conflicts of interest

There are no conflicts to declare.

Acknowledgements

This work was supported by the Zhejiang Outstanding Youth Fund (No. LR19E020004), the National Natural Science Foundation of China (No. 51572242, 11672269 and 11972323), the Zhejiang Provincial Natural Science Foundation of China (No. LR20A020002), the Opening Fund of State Key Laboratory for Strength and Vibration of Mechanical Structures (Xi'an Jiaotong University) (No. SV2018-KF-23), the Opening Fund of State Key Laboratory of Digital Manufacturing Equipment and Technology of Huazhong University of Science and Technology (No. DMETKF201817), the National Study Abroad Fund (No. 201908330181), and the Fundamental Research Funds for the Provincial Universities of Zhejiang (No. RF-B2019004).

Notes and references

1 Y. Wang, L. Wang, T. Yang, X. Li, X. Zang, M. Zhu, K. Wang, D. Wu and H. Zhu, *Adv. Funct. Mater.*, 2014, **24**, 4666–4670.
2 D. Y. Guo, Y. L. Su, H. Z. Shi, P. G. Li, N. Zhao, J. H. Ye, S. L. Wang, A. P. Liu, Z. W. Chen, C. R. Li and W. H. Tang, *ACS Nano*, 2018, **12**, 12827–12835.
3 C. Y. Wang, K. L. Xia, H. M. Wang, X. P. Liang, Z. Yin and Y. Y. Zhang, *Adv. Mater.*, 2019, **31**, 1801072.
4 Y. Zang, F. Zhang, C.-A. Di and D. Zhu, *Mater. Horiz.*, 2015, **2**, 140–156.
5 X. Wang, Y. Gu, Z. Xiong, Z. Cui and T. Zhang, *Adv. Mater.*, 2014, **26**, 1336–1342.
6 H. Tao, S.-W. Hwang, B. Marelli, B. An, J. E. Moreau, M. Yang, M. A. Brenckle, S. Kim, D. L. Kaplan, J. A. Rogers and F. G. Omenetto, *Proc. Natl. Acad. Sci. U. S. A.*, 2014, **111**, 17385–17389.
7 W. Z. Xu, Y. Xing, J. Liu, H. P. Wu, Y. Cui, D. W. Li, D. Y. Guo, C. R. Li, A. P. Liu and H. Bai, *ACS Nano*, 2019, **13**, 7930–7938.
8 S. Choi, S. I. Han, D. Kim, T. Hyeon and D. H. Kim, *Chem. Soc. Rev.*, 2019, **48**, 1566–1595.
9 H. Lee, T. K. Choi, Y. B. Lee, H. R. Cho, R. Ghaffari, L. Wang, H. J. Choi, T. D. Chung, N. Lu, T. Hyeon, S. H. Choi and D.-H. Kim, *Nat. Nanotechnol.*, 2016, **11**, 566–574.
10 Y. Khan, A. E. Ostfeld, C. M. Lochner, A. Pierre and A. C. Arias, *Adv. Mater.*, 2016, **28**, 4373–4395.
11 S. D. Zhang, H. Liu, S. Y. Yang, X. Z. Shi, D. B. Zhang, C. X. Shan, L. W. Mi, C. T. Liu, C. Y. Shen and Z. H. Guo, *ACS Appl. Mater. Interfaces*, 2019, **11**, 10922–10932.
12 W. Gao, H. Ota, D. Kiriya, K. Takei and A. Javey, *Acc. Chem. Res.*, 2019, **52**, 523–533.
13 D. Son, J. H. Kang, O. Vardoulis, Y. Kim, N. Matsuhisa, J. Y. Oh, J. W. F. To, J. Mun, T. Katsumata, Y. X. Liu, A. F. McGuire, M. Krason, F. Molina-Lopez, J. Ham, U. Kraft, Y. Lee, Y. J. Yun, J. B.-H. Tok and Z. N. Bao, *Nat. Nanotechnol.*, 2018, **13**, 1057–1065.
14 J. W. Chen, Q. L. Yu, X. H. Cui, M. Y. Dong, J. X. Zhang, C. Wang, J. C. Fan, Y. T. Zhu and Z. H. Guo, *J. Mater. Chem. C*, 2019, **7**, 11710.
15 A. P. A. Raju, A. Lewis, B. Derby, R. J. Young, I. A. Kinloch, R. Zan and K. S. Novoselov, *Adv. Funct. Mater.*, 2014, **24**, 2865–2874.
16 S. Riyajuddin, S. Kumar, S. P. Gaur, A. Sud, T. Maruyama, M. E. Ali and K. Ghosh, *Nanotechnology*, 2020, **31**, 295501.
17 X. R. Li, Y. Dai, Y. D. Ma, S. H. Han and B. B. Huang, *Phys. Chem. Chem. Phys.*, 2014, **16**, 4230–4235.
18 J. Park, Y. Lee, M. Ha, S. Cho and H. Ko, *J. Mater. Chem. B*, 2016, **4**, 2999–3018.
19 S. Gong, W. Schwalb, Y. Wang, Y. Chen, Y. Tang, J. Si, B. Shirinzadeh and W. Cheng, *Nat. Commun.*, 2014, **5**, 3132.
20 T. Tran Quang and N.-E. Lee, *Adv. Mater.*, 2016, **28**, 4338–4372.
21 C. Pang, T.-I. Kim, W. G. Bae, D. Kang, S. M. Kim and K.-Y. Suh, *Adv. Mater.*, 2012, **24**, 475–479.
22 M. Ha, S. Lim, J. Park, D.-S. Um, Y. Lee and H. Ko, *Adv. Funct. Mater.*, 2015, **25**, 2841–2849.
23 P. Nie, R. Wang, X. Xu, Y. Cheng, X. Wang, L. Shi and J. Sun, *ACS Appl. Mater. Interfaces*, 2017, **9**, 14911–14919.
24 M. Jian, K. Xia, Q. Wang, Z. Yin, H. Wang, C. Wang, H. Xie, M. Zhang and Y. Zhang, *Adv. Funct. Mater.*, 2017, **27**, 1606066.
25 X. Wu, Y. Han, X. Hang, Z. Zhou and C. Lu, *Adv. Funct. Mater.*, 2016, **26**, 6246–6256.
26 K. Takei, Z. Yu, M. Zheng, H. Ota, T. Takahashi and A. Javey, *Proc. Natl. Acad. Sci. U. S. A.*, 2014, **111**, 1703–1707.
27 J. Park, M. Kim, Y. Lee, H. S. Lee and H. Ko, *Sci. Adv.*, 2015, **1**, 1500661.
28 Y. Ma, K.-I. Jang, L. Wang, H. N. Jung, J. W. Kwak, Y. Xue, H. Chen, Y. Yang, D. Shi, X. Feng, J. A. Rogers and Y. Huang, *Adv. Funct. Mater.*, 2016, **26**, 5345–5351.
29 J.-Y. Hong, W. Kim, D. Cho, J. Kong and H. S. Park, *ACS Nano*, 2016, **10**, 9446–9455.
30 S. Han, M. K. Kim, B. Wang, D. S. Wie, S. Wang and C. H. Lee, *Adv. Mater.*, 2016, **28**, 10257–10265.
31 C.-L. Choong, M.-B. Shim, B.-S. Lee, S. Jeon, D.-S. Ko, T.-H. Kang, J. Bae, S. H. Lee, K.-E. Byun, J. Im, Y. J. Jeong, C. E. Park, J.-J. Park and U. I. Chung, *Adv. Mater.*, 2014, **26**, 3451–3458.
32 J. Park, Y. Lee, J. Hong, M. Ha, Y.-D. Jung, H. Lim, S. Y. Kim and H. Ko, *ACS Nano*, 2014, **8**, 4689–4697.
33 S. Wu, J. Zhang, R. B. Ladani, A. R. Rayindran, A. P. Mouritz, A. J. Kinloch and C. H. Wang, *ACS Appl. Mater. Interfaces*, 2017, **9**, 14207–14215.

34 H. Jang, Y. J. Park, X. Chen, T. Das, M. S. Kim and J. H. Ahn, *Adv. Mater.*, 2016, **28**, 4184–4202.

35 Y. Cheng, R. Wang, J. Sun and L. Gao, *Adv. Mater.*, 2015, **27**, 7365–7371.

36 H.-B. Lee, C.-W. Bae, L. T. Duy, I.-Y. Sohn, D.-I. Kim, Y.-J. Song, Y.-J. Kim and N.-E. Lee, *Adv. Mater.*, 2016, **28**, 3069–3077.

37 J. Ren, C. Wang, X. Zhang, T. Carey, K. Chen, Y. Yin and F. Torrisi, *Carbon*, 2017, **111**, 622–630.

38 K. N. Kudin, B. Ozbas, H. C. Schniepp, R. K. Prud'homme, I. A. Aksay and R. Car, *Nano Lett.*, 2008, **8**, 36–41.

39 J. Kuang, L. Liu, Y. Gao, D. Zhou, Z. Chen, B. Han and Z. Zhang, *Nanoscale*, 2013, **5**, 12171–12177.

40 X. Xu, R. Wang, P. Nie, Y. Cheng, X. Lu, L. Shi and J. Sun, *ACS Appl. Mater. Interfaces*, 2017, **9**, 14273–14280.

41 S.-Z. Guo, K. Qiu, F. Meng, S. H. Park and M. C. McAlpine, *Adv. Mater.*, 2017, **29**, 1701218.

42 Q. Wang, M. Jian, C. Wang and Y. Zhang, *Adv. Funct. Mater.*, 2017, **27**, 1605657.

43 K. S. Kim, H. J. Lee, C. Lee, S. K. Lee, H. Jang, J. H. Ahn, J. H. Kim and H. J. Lee, *ACS Nano*, 2011, **5**, 5107–5114.

44 L. Sheng, Y. Liang, L. Jiang, Q. Wang, T. Wei, L. Qu and Z. Fan, *Adv. Funct. Mater.*, 2015, **25**, 6545–6551.

45 H.-B. Yao, J. Ge, C.-F. Wang, X. Wang, W. Hu, Z.-J. Zheng, Y. Ni and S.-H. Yu, *Adv. Mater.*, 2013, **25**, 6692–6698.

46 S. Gong, D. T. H. Lai, B. Su, K. J. Si, Z. Ma, L. W. Yap, P. Guo and W. Cheng, *Adv. Electron. Mater.*, 2015, **1**, 1400063.

47 I. You, B. Kim, J. Park, K. Koh, S. Shin, S. Jung and U. Jeong, *Adv. Mater.*, 2016, **28**, 6359–6365.